Ultrasensitive and Visible Detection of Influenza A Virus Based on Enzymatic Properties of Layered Gold Nanoparticles

Eunji Jeong, Geunseon Park, Jinyoung Kim, Sojeong Lee, Chaewon Park, Jong-Woo Lim, Minjoo Yeom, Daesub Song, and Seungjoo Haam**

E. Jeong‡, Dr. G. Park‡, Dr. J. Kim, Lee, S, Dr. C. Park, Prof. S. Haam
Department of Chemical and Biomolecular Engineering, Yonsei University, Seoul 03722, Republic of Korea
E-mail: haam@yonsei.ac.kr

Dr. J-W. Lim, Dr. M. Yeom, Prof. D. Song
College of Veterinary Medicine and Research Institute for Veterinary Science, Seoul National University, Seoul 08826, Republic of Korea
E-mail: sds@snu.ac.kr

Dr. G. Park‡
Department of Chemical Engineering, University of Michigan, Ann Arbor, Michigan 48109, United States

‡E. Jeong and G. Park contributed equally to this work.

Keywords: gold nanoparticle, avidin-biotin binding, nanozyme effect, signal amplification, influenza A virus detection, point-of-care diagnostic

Author Manuscript

This is the author manuscript accepted for publication and has undergone full peer review but has not been through the copyediting, typesetting, pagination and proofreading process, which may lead to differences between this version and the Version of Record. Please cite this article as doi: 10.1002/sstr.202300380.

This article is protected by copyright. All rights reserved

Abstract

Considering the urgent demand for reliable and rapid detection of infectious respiratory viruses during unpredictable pandemics, an innovative ultrasensitive colorimetric immunoassay for influenza A (H1N1) virus detection was developed in this study. The proposed approach leverages dual amplification by combining layer-by-layer interactions with the nanozyme effect of biotinylated gold nanoparticles (BGNPs). BGNPs assemble around the target via repeated incubation cycles under optimized conditions, resulting in a layered structure that increases optical density, producing a more intense signal proportional to the viral titer. Additionally, the nanozyme effect of the layered BGNPs induces oxidation of 3,3',5,5'-tetramethylbenzidine, which further enhances the visible signal detectable by the naked eye. This synergetic nanoprobe-based system demonstrates remarkable sensitivity, with a limit of detection of $10^{1.29}$ EID_{50}/mL, which is 2,500-fold higher than that of commercial rapid kits and conventional enzyme-linked immunosorbent assays, within a rapid 55-minute timeframe. Furthermore, the anti-interference capability and portability of the developed system reinforce its practicality, making it a promising tool for field diagnostic tests that offers advanced, ultrasensitive, and early detection of respiratory viruses.

Author Manuscript

1. Introduction

This article is protected by copyright. All rights reserved

In recent decades, numerous crises have been caused by unpredictable infectious diseases attributable to respiratory viruses. Pandemics stemmed from influenza A viruses (IAVs), such as the Hong Kong flu caused by H3N2 in 1968 and swine flu caused by H1N1 in 2009, have inflicted significant damage to public health.[1,2] The most recent global health crisis was triggered by the emergence of the severe acute respiratory syndrome coronavirus 2 in early 2020, which resulted in over 14.9 million deaths and widespread disruption.[3] Experts widely believe that the next pandemic will likely be driven by zoonotic diseases, considering historical precedents and the fact that approximately 60.3% of new infectious diseases are zoonotic in origin.[4,5] In this context, IAVs pose a particularly high risk due to their ability to infect multiple host species and undergo antigenic drift.[6–8] Timely and accurate diagnosis of IAV infections is therefore crucial for effective disease management, reducing transmission, and pandemic prevention.[9,10]

Real-time quantitative polymerase chain reaction (RT-qPCR) is regarded as the gold standard among existing diagnostic tools, and has played a crucial role in pandemics owing to its high accuracy and sensitivity.[11] However, RT-qPCR can only be performed by trained professionals and requires a substantial amount of time, making it less than ideal for use in fields where rapid diagnosis and immediate isolation of infected individuals are required to prevent further infection.[12,13] Thus, there is an urgent need for rapid and simple point-of-care testing (POCT) solutions to address these limitations in a way that mitigates the delay involved in transferring clinical specimens to specialized facilities for timely decision-making regarding isolation and treatment interventions.[14] Consequently, numerous studies are in progress to advance POCT technologies.[15-17] Representatively, Zeng's group presented an electrochemical immunoassay for POC detection of the SARS-CoV-2 N protein. And they developed a portable photoelectrochemical detection system for human papillomavirus-16 (HPV-16) using CRISPER-Cas12a system. They utilized a smartphone for visual readout, enabling rapid, highly sensitive, and portable measurement of the target biomolecule.[18,19] Immunodiagnostic methods based on host-guest interactions, such as lateral flow assays (LFAs) based on colloidal gold

This article is protected by copyright. All rights reserved

Author Manuscript

nanoparticles (GNPs), have been utilized as rapid diagnostic tests, as they offer simplicity, rapid turnaround times, and ease of interpretation.[20] Although LFAs are powerful tools for POCT, they do have limitations, such as low sensitivity and weak detection signal intensity. This is because the detection signal in the test line relies on a single substitutional binding between the colloidal gold-conjugated antibody and the target and is only detected when the signal from that binding exceeds a certain threshold. Therefore, new POCT technologies that identify low-abundance biomarkers in the early stages of infection and improve sensitivity through signal generation and enhancement are required as alternatives to existing diagnostic technologies, which have limited field use, low sensitivity, and a tendency for false negatives that prevent the development of effective control measures.[21,22]

The detection of target biomolecules with high-intensity signals is critical to the performance of immunosensors. Researchers have explored various signal amplification strategies using nanomaterial-based signal-generating reporters. For instance, Huang et al. reported an immunosensor utilizing gold nanoparticles self-assembled around a target, and Lin et al. developed a gold nanorod probe for electrochemical sensing based on a superstructure immunocomplex. [23,24] These systems achieved high optical densities by converting a single target binding event into a cascade of numerous signaling molecule bindings. Therefore, the assembly of particles resulted in a more pronounced expression for signal, enabling highly sensitive target diagnosis.

Another approach involves the use of nano-biocatalysts to enhance the intensity of the signal generated by the target detection events; this approach primarily involves the use of enzyme complexes and inorganic nanomaterials with enzyme-like activity. Representatively, Yu et al. reported that paper electrode-based flexible pressure sensor for POC of carcinoembryonic antigen using platinum nanozyme which can efficiently catalyze the decomposition of H_2O_2 to O_2.[25] Additionally, they presented a strategy for implementing signal amplification and developing ultrasensitive non-enzymatic biosensors based on hollow Prussian blue nanoparticles with their

This article is protected by copyright. All rights reserved

Author Manuscript

enzyme-like peroxidase activity.[26] These researches have enabled considerable progress in the effective amplification of target substance detection signals by actively utilizing the enzymatic properties of nanomaterials. They also have achieved signal amplification with lower costs and greater stability compared to artificial enzymes. However, major barriers persist in controlling the sensitivity of nano-biocatalysts and in addressing false signal amplification due to nonspecific adsorption. Therefore, meticulous engineering of the structure and surface properties of nanoprobes is necessary to achieve high specificity for target substances and to maximize catalytic activity.[27]

To address the need for a highly sensitive point-of-care influenza virus detection system with effective signal amplification, we developed a diagnostic system that leverages the unique properties of GNPs, which are well-suited for surface engineering applications and exhibit strong catalytic activity. Especially, the unique surface property of GNPs, localized surface plasmon resonance (LSPR), generates a strong optical signal, which is advantageous to optimize nanoparticles through sophisticated analysis. Simultaneously, ease of surface modification can be used to stably conjugate the desired biomolecules to the surface of the GNP. Therefore, we chose GNPs as signal probes, as all of their characteristics were beneficial for our intended system.[28,29] Our system comprises a signal amplification mechanism involving layer-by-layer (LBL) assembly of avidin-linked biotinylated gold nanoparticles (BGNPs) that utilizes the strong biotin-avidin binding affinity.[30,31] This LBL assembly strategy mediates target-specific events into a densely stacked configuration of BGNPs, significantly boosting signal output and consequently enhancing the sensitivity of the diagnostic system. Additionally, the layered BGNPs exhibit peroxidase-like activity, leveraging a catalytic property known as the nanozyme effect to further amplify the target-specific detection signal.[32,33] This dual amplification strategy combines precise control of the surface properties of GNPs, target-specific amplification via avidin-biotin interactions, and the nanozyme effect, resulting in visible signal detection within a 1-h timeframe. Furthermore, our diagnostic system streamlines the process by eliminating the need for lysis pretreatment, and has the advantage of being able to detect intact viruses.

Author Manuscript

This article is protected by copyright. All rights reserved

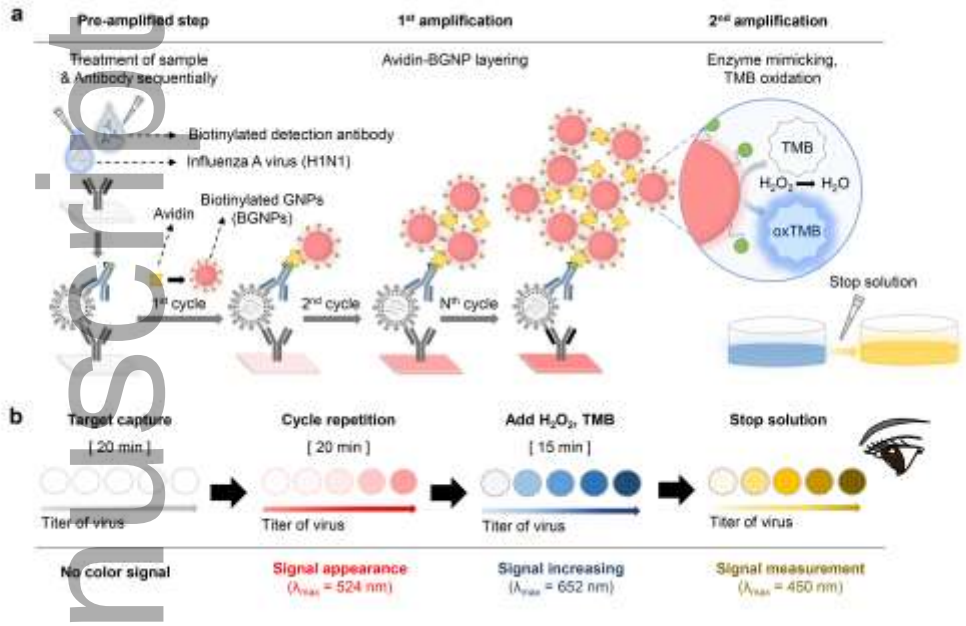
By detecting the virus in its intact form, our system mitigates the risk of false-positive signals caused by residual nucleic acids that can remain in the body even after the virus has ceased to cause an infection.[34] This aspect addresses a limitation of conventional PCR-based nucleic acid diagnostic technologies, thereby complementing existing methods to more accurately assess active viral infections with increased precision and reliability. Our diagnostic assay involving dual-signal amplification achieved high sensitivity and selectivity without the need for further specimen processing and demonstrated outstanding sensitivity than other GNP-based and existing commercialized LFAs, underscoring its suitability as a robust POCT for virus detection.

Author Manuscript

This article is protected by copyright. All rights reserved

2. Results and Discussion

2.1. Working Principle of LBL Signal Amplification Using BGNPs



Scheme 1. Working principle of layer-by-layer (LBL) signal amplification using biotinylated GNPs (BGNPs). (a) Schematic representation of the two-step colorimetric signal amplification for the detection of influenza A virus. Dual signal amplification comprised layer-by-layer accumulation of BGNPs via avidin-biotin interaction, and enzyme mimicking 3,3',5,5'-tetramethylbenzidine (TMB) oxidation of the accumulated BGNPs. (b) Workflow for the quantitative detection and serial color change within 55 min at room temperature (25 °C).

The LBL signal amplification system presented in this study operates based on the principles of antigen-antibody interaction, avidin-biotin binding, and nanozyme activity of BGNPs, as shown in **Scheme 1**. The assay comprised three consecutive steps, the first of which involved capturing the target virus. In this step, the viral sample and biotinylated polyclonal antibody were introduced sequentially to the plate where the monoclonal capture antibody was immobilized, resulting in the formation of a biotinylated sandwich complex via host-guest interactions. These binding events led to the formation of a substructure, that is, BGNP accumulation, with avidin functioning as a bridge at the first amplification step. The repeating cycle number of sequential avidin and BGNP treatments determined the amplification level in the red signal at a maximum absorbance peak (λ_{max}) of 524 nm.

This article is protected by copyright. All rights reserved

Author Manuscript

The intensity of the red hue on the plate showed dose-response signal production, enabling naked-eye detection. This color indicates the assembly of BGNPs around the target as a result of the first amplification, thereby correlating with the viral titer of IAV. The second amplification step, the catalytic signal-increasing stage, was induced by the enzyme-mimicking properties of the BGNPs. Upon exposure to hydrogen peroxide (H_2O_2), the BGNPs catalyze the oxidation of colorless 3,3',5,5'-tetramethylbenzidine (TMB) to emit an intensified blue color signal. During this amplification stage, a more enhanced intensity of the blue color was observed, surpassing the red color emitted previously. After processing H_2O_2 and TMB incubation for 15 minutes at room temperature is completed, a stop solution was used to terminate the enzymatic reaction of the BGNPs. Through this procedure, the oxidation of TMB was stopped and the signal appeared in yellow. These sequential steps generated an amplified signal proportional to the target amount by forming a supramolecular structure of the BGNP probe, acting as a nanozyme, near the target virus. Therefore, as illustrated in Scheme 1b, each stage of the process generates a visible signal that can be measured and discerned with the naked eye. The overall detection process involves capturing the target virus, layering the BGNPs to generate a detection signal, and using the nanoenzymatic properties of the BGNPs to enhance the signal, all of which can be completed within 55 min at room temperature (25 °C).

Author Manuscript

This article is protected by copyright. All rights reserved

2.2. Nanozyme Activity of BGNPs

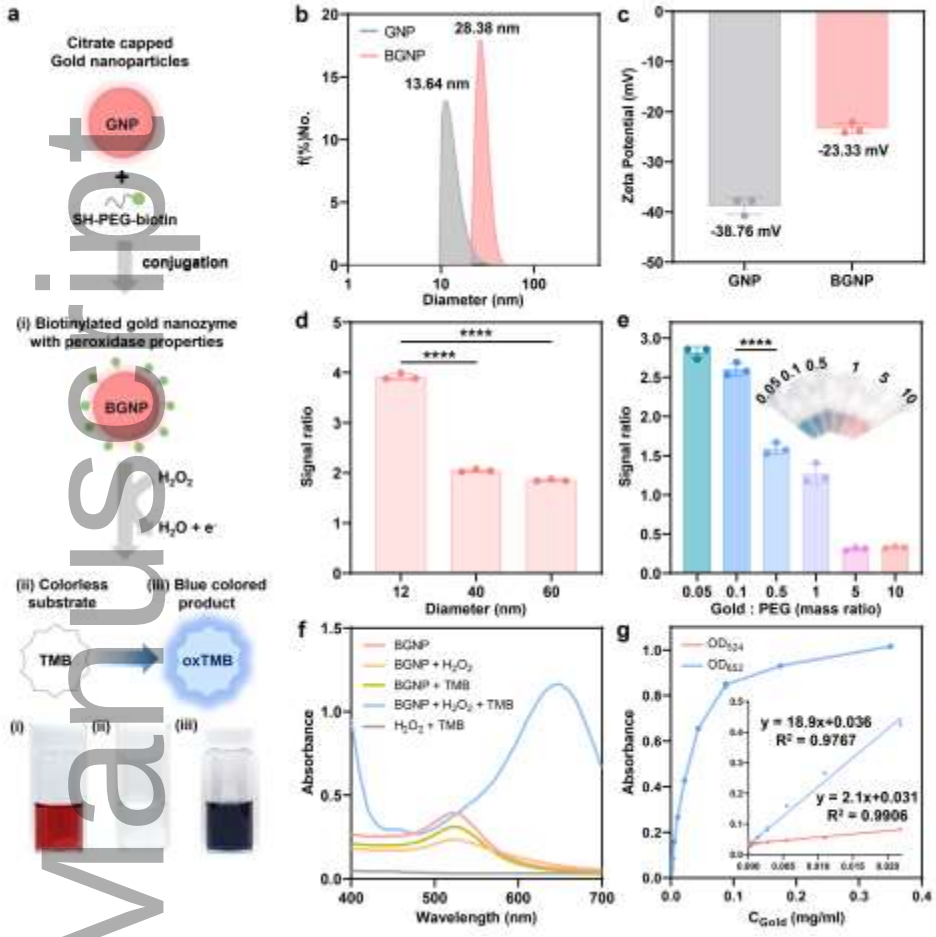


Figure 1. Nanozyme activity of biotinylated gold nanoparticles (BGNPs). (a) Schematic representation of BGNP synthesis and their nanozyme activity. Characterization of GNPs and BGNPs are presented with (b) size distribution, (c) zeta potential. Optical density ratio (signal ratio) of BGNPs at 524 (OD_{524}) and 652 nm (OD_{652}) for nanozyme activity evaluation are shown as a function of (d) the diameter of the GNPs and (e) the conjugated mass ratio of the biotin PEG thiol (SH-PEG-biotin) and gold ions comprising the GNPs. (f) UV-visible spectrum of BGNPs for evaluating the nanozyme activity of the BGNPs, BGNP alone (red) or containing H_2O_2 (orange), 3,3',5,5'-tetramethylbenzidine (TMB) (green), H_2O_2+TMB (blue) and H_2O_2+TMB (gray). (g) The calibration curves for OD_{524} and OD_{652} are presented in relation to the concentration of gold ions (C_{gold}) in BGNP. Significant differences are denoted by the asterisks with *p* values (****p <0.0001). Data (c)-(g) represent mean ± standard deviation with n=3.

For successful signal amplification and sensitive viral detection, the surface properties of the BGNPs were thoroughly examined to determine their avidin-assisted BGNP layering effect and enzymatic

This article is protected by copyright. All rights reserved

Author Manuscript

activity. BGNPs were prepared by capping the GNPs with biotin PEG thiol (SH-PEG-biotin), which acts as a peroxidase upon the addition of H_2O_2 and TMB, as shown in **Figure 1a.** GNP biotinylation is essential for avidin-bridged accumulation, the first signal amplification stage. However, excessive biotinylation may overly cover the surface of GNPs, causing unnecessary impedance of the peroxidase-like characteristics of BGNPs, which are essential for the second signal amplification stage. To perform the proposed assay, we synthesized and characterized GNPs and BGNPs. The PEG brushes on the BGNPs increased their hydrodynamic radii and zeta potentials, imparting colloidal stability and a neutral capping layer **(Figure 1b and 1c)**.[35] The characteristic peak shift from 520 to 524 nm without any aggregation confirmed the successful synthesis of BGNPs **(Figure S1a)**.[36,37] During the biotin-capping process, the BGNPs maintained their spherical morphology and monodispersity **(Figure S1b)**. The capping of SH-PEG-biotin in the GNP was confirmed by identifying the characteristic absorption peaks of PEG and biotin using Fourier-transform infrared (FTIR) and nuclear magnetic resonance (NMR) spectroscopy **(Figure S2)**. Instead of directly conjugating biotin to the GNPs, we utilized PEG chains as linkers to provide colloidal stability and prevent the aggregation of the GNPs, which can be induced by various salts or proteins in the biological environment. The colloidal stability of BGNPs was investigated in NaCl, phosphate-buffered saline (PBS), and 0.3% bovine serum albumin (BSA) buffer conditions. The aggregation level was assessed by calculating the ratio of the absorbance peaks at 520 (OD_{520}) and 630 nm (OD_{630}) based on the properties of the GNPs. Upon aggregation, the absorbance spectrum was found to be accompanied by a red shift (**Figure S3**).[38] These results showed that the BGNPs maintained their original red color and absorbance spectrum with a low absorbance ratio (OD_{630}/OD_{524}), whereas GNPs exhibited a color change to gray and an increase in the absorbance ratio (OD_{630}/OD_{520}) in NaCl and PBS buffer conditions, indicating aggregation.[39] In summary, we synthesized BGNPs with high colloidal stability in a biological environment that successfully enhanced LBL signal amplification.

Author Manuscript

This article is protected by copyright. All rights reserved

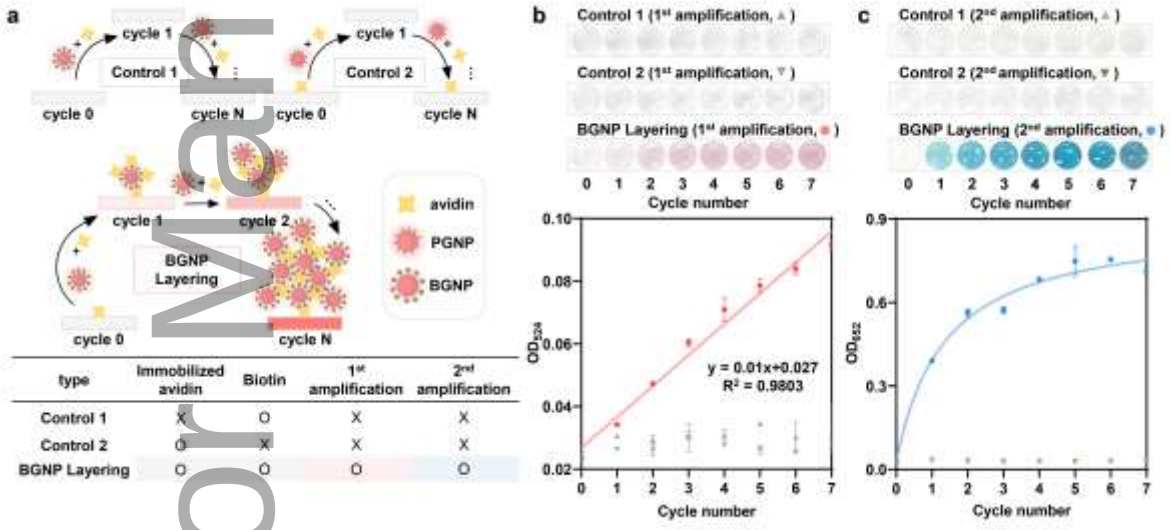
Subsequently, we conducted the meticulous optimization of BGNPs to promote their enzyme-mimicking properties. As BGNP-mediated TMB oxidation occurs on the BGNP surface, the surface area and degree of accessibility of the substrate to the exposed surface are important factors in determining the efficiency of detection signal amplification.[40] In this regard, the diameter of the GNPs and the SH-PEG-biotin capping ratio were considered the main factors affecting the nanozyme effect of BGNPs. We prepared GNPs with diameters of 40 and 60 nm, which showed λ_{max} of 530 and 540 nm respectively, to compare and optimize the nanozyme activity of 12-nm GNPs **(Figure S4)**. We added TMB and H_2O_2 to each GNP solution and calculated the degree of oxidation from the signal ratio (optical density [OD] at λ_{652nm} / OD at λ_{max} of each particle). GNPs showed a higher signal ratio at smaller sizes owing to an increased ratio of volume to surface area, with smaller GNPs providing a larger active site while containing the same amount of gold. **(Figure 1d)**.[41] GNPs of all three sizes exhibited TMB oxidation, but notably, 12-nm GNPs demonstrated comparatively heightened efficiency with a signal ratio of 3.99. In contrast, GNPs of other sizes failed to attain this level of reactivity. Therefore, we selected 12-nm GNPs that showed the highest TMB oxidation for the target detection experiments. The signal ratio of BGNP-mediated TMB oxidation was then examined at different BGNP and SH-PEG-biotin capping ratios, and the results are shown in **Figure 1e.** The BGNP capping ratio was calculated based on the mass ratio of gold to PEG-biotin, and BGNP showed the highest TMB oxidation at a 1:0.1 mass ratio of gold to PEG-biotin, which was determined to be the optimal secondary amplification activity condition. Furthermore, we determined the optimal concentration of substrates, including H_2O_2 and TMB, and the incubation time with BGNPs to maximize the signal **(Figure S5).** For H_2O_2 concentration, a value of 5 M, which exhibited a sharp difference from the previous concentration range, was selected. Additionally, to maximize the signal, the highest concentration of TMB used as a substrate was optimized for incubation at 15 minutes, corresponding to the saturation time for OD_{652}.

Author Manuscript

This article is protected by copyright. All rights reserved

Then, we examined the nanozyme activity of BGNPs**.** As shown in **Figure 1f**, the BGNPs produced a visible signal at 652 nm under enzymatic reaction conditions requiring both H_2O_2 and TMB. The BGNP-induced TMB oxidation is highly specific to certain conditions and generates a more intense signal than BGNPs at 524 nm, which is advantageous for detecting trace amounts of targets. As shown in **Figure 1g,** we confirmed that BGNP-induced TMB oxidation and BGNP concentration showed a strong linear relationship, which implies that the BGNPs accumulated after the target-capture and layering stages of BGNPs will accelerate detection signal amplification.

2.3. Evaluation of First and Second Amplification on the Avidin Immobilized Plate



type	Immobilized avidin	Biotin	1st amplification	2nd amplification
Control 1	X	O	X	X
Control 2	O	X	X	X
BGNP Layering	O	O	O	O

Figure 2. Evaluation of first and second amplification on the avidin immobilized plate. (a) Schematic representation of the biotinylated gold nanoparticle (BGNP)-based layer-by-layer (LBL) primary amplification process involving specific recognition of avidin-biotin. Control 1 : avidin non-immobilized well and BGNP pair; Control 2 : avidin immobilized well and PEGylated GNP (PGNP) pair; BGNP layering: avidin immobilized well and BGNP pair. The lower table presents the predicted results of first and second amplification in the presence or absence of avidin and biotin. (b) First amplification at three cases after each cycle from 0 to 7 (upper). Plots of the OD_{524} recorded from upper image (lower). (c) Second amplification at three cases after each cycle from 0 to 7 (upper). Plots of the OD_{652} recorded from upper image (lower). Data (b) and (c) represent mean ± standard deviation with n=3.

This article is protected by copyright. All rights reserved

Author Manuscript

After establishing the optimal BGNP conditions for stable nanozyme activity in a biological detection environment, we explored strategies to amplify the detection signal through effective layering with BGNPs. In the layering process based on the bridging of avidin and BGNP, steric hindrance, which is affected by the length of the PEG chain and SH-PEG-biotin grafting density, was thought to be the main factor determining performance.[37, 42] To verify this, BGNPs were fabricated using SH-PEG-biotin polymers with molecular weights of 0.4, 1, 3.4, and 5 kDa. The grafting density of SH-PEG-biotin on the BGNP surface was analyzed via thermogravimetric analysis (TGA), and was found to decrease with increasing polymer chain length **(Table S1a).** This result was attributed to an increase in conformational entropy as the chain length of the PEG molecule increased; consequently, the number of SH-PEG-biotin molecules grafted onto the GNPs decreased with increasing PEG molecular weight.[35] As the avidin-BGNP binding event is strongly influenced by the number of biotin molecules, the extent of SH-PEG-biotin capping of BGNP can be a determinant of the layering efficiency. We observed that the lower the PEG molecular weight, the higher the BGNP-derived OD_{524} in multiple repeated cycles of BGNP accumulation **(Figure S6a and Table S1b)**. We further assessed the TMB oxidation efficiency of the accumulated BGNPs at cycle 4 and found that BGNPs capped with lower PEG molecular weights potentiated a higher level of TMB oxidation (OD_{652}) **(Figure S6b)**. Even though short PEG chains in SH-PEG–biotin showed the highest signal production, BGNPs prepared with 0.4 kDa PEG chain length exhibited a slightly aggregated absorbance spectrum **(Figure S7)**. This can be explained by the fact that the colloidal stability of BGNPs, provided by PEG-derived steric hindrance, is insufficient in the 0.4 kDa PEG chains, resulting in the aggregation of BGNPs.[43] These results led us to select SH-PEG-biotin with a molecular weight of 1 kDa to maximize both the detection efficiency and the stability of BGNPs.

Following the demonstration of the signal amplification strategy, we assessed the nonspecific binding effect in the process associated with the potential risk of false positives. The BGNP layering

This article is protected by copyright. All rights reserved

Author Manuscript

process was tested and compared with two control groups for direct comparison: layering of BGNPs without primary avidin immobilization (control 1) and layering of GNPs capped with thiol biotin (SH-PEG) to obtain PEGylated GNPs (PGNPs) with primary avidin immobilization (control 2) **(Figure 2a)**. For these three cases, the absorbance was monitored at OD_{524} of BGNP and OD_{652} of BGNP-mediated TMB oxidation in repetitive cycle numbers from 0 to 7. First, to determine the optimal detection time, we tested three layering processes at different incubation times in a cycle, ranging from 1 to 15 min, for avidin and BGNPs. As the incubation time increased, the BGNP layering process produced a higher-intensity signal, with OD_{652} signal exposure being particularly strong from 5 min onwards **(Figure S8)**.

To assess the correlation between BGNP accumulation and TMB oxidation, H_2O_2 and TMB were treated after each cycle and incubated together. In contrast to the two controls, BGNP layers with primary avidin immobilization showed continuous signal amplification and a positive correlation as the number of cycles increased. The nanozyme effect was observed to vary depending on the amount of accumulated BGNPs, resulting in strong optical densities at OD_{524} and OD_{652}, emitting vivid red and blue colors visible to the naked eye, respectively. This result was attributed to the assembly of BGNPs by avidin-biotin binding, whereas in controls 1 and 2, the cycle failed to initiate the layering process because of the absence of primary avidin immobilization and biotin capping on the GNPs, respectively, resulting in an absence of signal production in either control **(Figure 2b and 2c)**. This suggests that layering of BGNPs occurs without nonspecific adsorption and that an amplified signal can only be obtained in the presence of the target. This demonstrates that our diagnostic assay can achieve quantitative detection using amplified signals. Notably, in the case of BGNPs layering at cycle 1, the color signal is emitted from the BGNPs monolayer formed by avidin, but from cycle 2 onwards, as avidin and BGNPs are processed over the monolayer, a much stronger signal is gradually observed due to the formation of a larger assembly. This multilayer structure

Author Manuscript

This article is protected by copyright. All rights reserved

mediated by increase in the number of BGNPs induces a more active nanozyme effect and contributes to second signal amplification.

2.4. Virus Detection Analysis

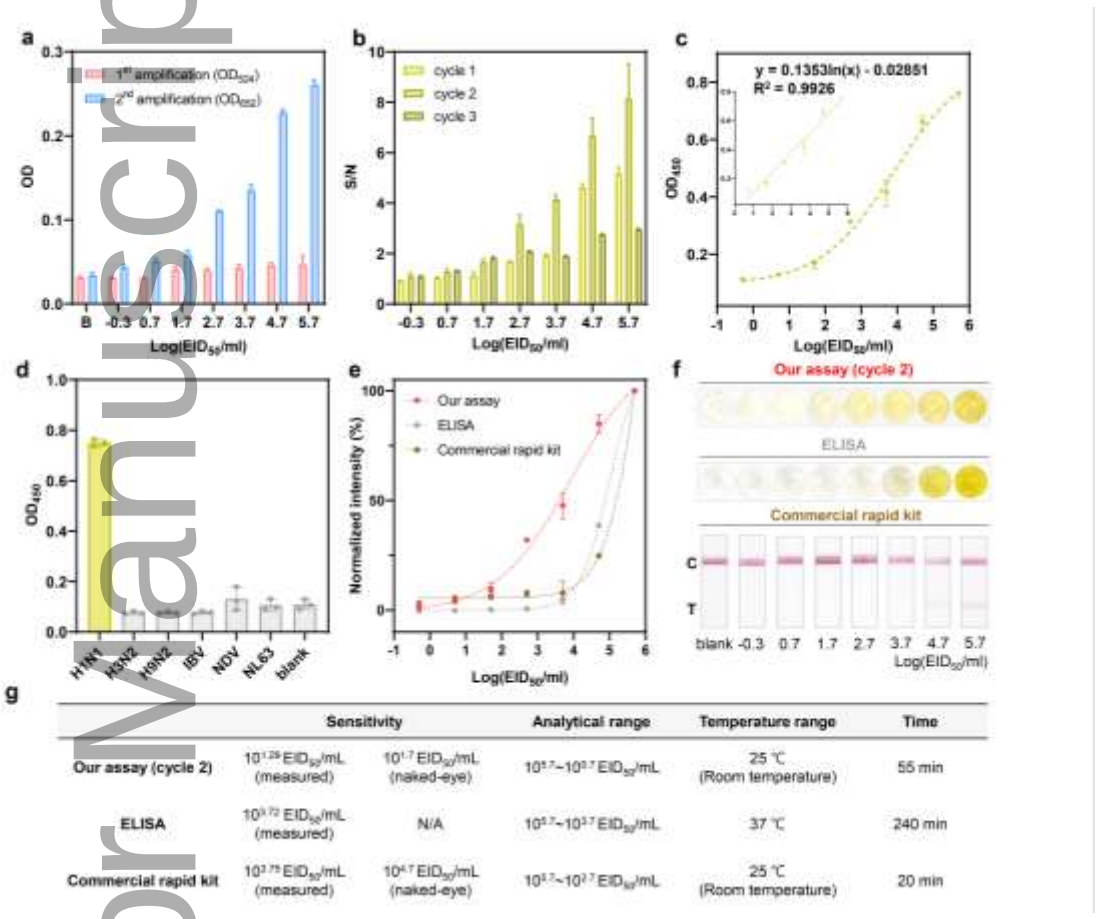


Figure 3. Virus detection analysis. (a) Detection signal at the first and second amplification under cycle 2 presented according to the virus titer. (b) Signal-to-noise (S/N) value for each cycle from 1 to 3 were calculated and plotted by dividing the signal from each titer condition by the signal from the blank. (c) The influenza A virus (IAV) detection signal at cycle 2 showed a linear relationship with viral titer over the analytical range. (d) The specificity analysis of the assay against a range of respiratory viruses was conducted at cycle 2. The virus samples tested had the following titers: H1N1 had a titer of $10^{5.7}$ EID_{50}/mL; and H3N2, H9N2, Influenza B virus (IBV), Newcastle disease virus (NDV), and human coronavirus (NL63) had titers of $10^{7.25}$ EID_{50}/mL, $10^{5.7}$ EID_{50}/mL, $10^{4.25}$ EID_{50}/mL, $10^{7.5}$ EID_{50}/mL, and $10^{4.1}$ $TCID_{50}$/mL, respectively. (e) S/N value of our assay and conventional methods were plotted according to the virus titer. Each value was normalized after subtracting the blank from each readout-signal intensity. (f) Comparison of the results of H1N1

This article is protected by copyright. All rights reserved

Author Manuscript

detection using our assay at cycle 2 with those from conventional diagnostic assays (ELISA and a commercial rapid kit) A gray background indicates that it is discernible to the naked eye in our assay. (g) Comparison of our assays with conventional diagnostic assays. The limits of detection (LOD) for our assay and ELISA were determined using the OD_{450} read-out signal obtained from a microplate. Data (a)-(e) represent mean ± standard deviation with n=3.

This diagnostic system utilizes a sandwich complex that includes target capture and signal amplification based on host-guest interactions to detect IAVs.[44] To evaluate this complex, immunowells were coated with an H1N1-specific monoclonal capture antibody, and BSA was used to block the remaining empty space and prevent nonspecific adsorption. We speculated that upon loading the targeted IAVs into the prepared wells, the IAVs were captured and formed sandwich complexes that sequentially bound with a biotinylated detection antibody (dAb). The preparation and sandwich complex formation stages were confirmed by image analysis using atomic force microscopy (AFM) **(Figure S9).** The successful formation of the sandwich complex not only plays an important role in target capture but also implies that biotin is present on the surface of the complex for subsequent detection signal amplification stages. Optimization of the conditions that increase the signal-to-noise ratio (S/N) is essential to maximize signal intensity and achieve high sensitivity for IAV detection. Therefore, before evaluating the sensitivity, we selected and tuned several important factors, including the incubation time of the target and dAb, ratio of BGNPs to treated avidin in each cycle, and BGNP concentration **(Figure S10)**. Short turnaround times are important in point-of-care diagnostics; as sensitivity and turnaround time are generally tradeoffs, it is important to find a balance between the two factors in the development of point-of-care diagnostics.[45] After evaluating the sensitivity of the assay under different incubation time conditions for virus capture, we determined that an incubation time of 10 min was optimal for obtaining high S/N values and did not overly increase the overall detection time **(Figure S10a)**. Furthermore, we determined that a key factor for maximizing the signal and minimizing nonspecific adsorption was the concentration of BGNP and avidin added in each cycle for a layering effect. We investigated the S/N values of the H1N1 detection

This article is protected by copyright. All rights reserved

Author Manuscript

results for various molar ratios of avidin to biotin coated on multiple concentrations of BGNPs **(Figure S10b and S10c)**. We selected a molar ratio of avidin to biotin of 1:2 and a BGNP concentration of 0.15 mg/ml as the optimal conditions to achieve high S/N values. Under carefully optimized conditions, the accumulation of BGNPs around the captured virus at each cycle was confirmed by scanning electron microscopy (SEM) at $10^{5.7}$ EID_{50}/mL H1N1. And it was confirmed that a larger assembly of BGNPs was formed in cycle 2 compared to that in cycle 1 **(Figure S11)**.

Subsequently, we evaluated the sensitivity of our assay to H1N1 stock solution. The detection results of each amplification stage in repetitive cycles 1–3 were measured and photographed **(Figure 3a and S12)**. We observed that the values of OD_{524} and OD_{652} increased with virus titer, indicating that each amplification was successful and provided a dose-response read-out signal, enabling quantitative target virus detection. Notably, the signal in the blank wells showed a significantly lower OD value, indicating that the assay generated a visible detection signal specific for the formation of a complex of the target virus, detection antibody, and avidin-BGNP bridges. For secondary amplification, the reaction was stopped by adding stop solution (5 M sulfuric acid [H_2SO_4]) after 15 min of TMB oxidation. Subsequently, we calculated the S/N values of the test results from cycles 1 to 3 and obtained a high S/N value in cycle 2, which was selected as the optimal repetitive cycle for H1N1 detection **(Figure 3b)**. Notably, the S/N of cycle 3 is lower than that of cycle 2. This outcome arises from an optimization process that considers the trade-off relationship between reducing the time required for detection and maximizing diagnostic signals. Consequently, the diagnostic signal greatly increased as the number of cycles increased, but it was inevitable that background signal would be also slightly generated. In the dual amplification step from cycles 1 to 3, the calibration curves determined the limit of detection (LOD) for each cycle **(Figure S13)**. Additionally, we used measurement tools, including ImageJ software 1.47v and the RGB Color Detector application (Android), to analyze the detection results considering visible detection situations (**Figure S14, S15, and S16)**. An LOD of $10^{1.29}$ EID_{50}/ml was measured by the

This article is protected by copyright. All rights reserved

Author Manuscript

microplate reader in cycle 2, indicating considerably higher sensitivity compared to other infectious virus diagnostic approaches that employ inorganic materials for colorimetric detection **(Table S2)**. The linear dependence between OD_{450} and the titer of the target virus in **Figure 3c** also suggests that quantitative detection with good regression is possible over a wide dynamic range ($10^{5.7}$–$10^{0.7}$ EID_{50}/mL) encompassing preclinical to symptomatic patients. Additionally, we compared the detection performance of different measurement tools **(Table S3)** and found that they all had a wide analytical range with high correlation and similar LOD levels. Notably, the photographed test results measured using the smartphone application showed the lowest LOD ($10^{0.68}$ EID_{50}/mL) in cycle 2, suggesting the applicability of this system for point-of-care diagnosis.

High selectivity to detect only the target virus is essential to address the potential risk of obtaining false-positive results in this diagnostic system. Therefore, we investigated the selective diagnostic ability of our BGNP-layering detection system for IAV **(Figure 3d and S17)**. Target H1N1 virus and other non-target viral strains (H3N2, H9N2, Influenza B virus, Newcastle disease virus, human coronavirus, and blank (PBS. as negative controls)) were evaluated under the same conditions. In cycles 1 and 2, we observed visible detection of the target virus, H1N1, whereas no visible detection signal was generated for the other non-target viruses, confirming that our system could specifically detect IAV based on the serial amplification of BGNPs.

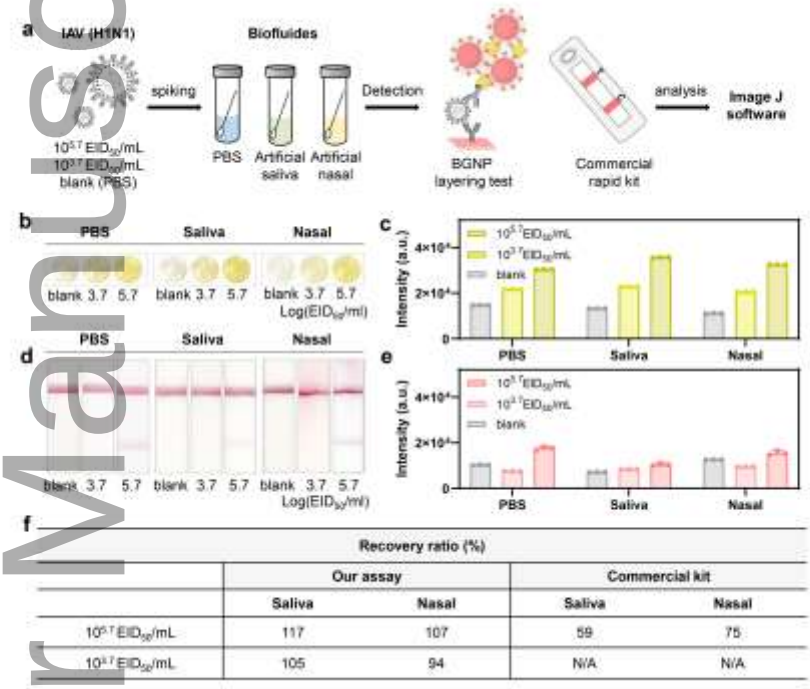
Furthermore, to validate the superiority of the developed diagnostic system over existing approaches, we compared its detection performance with that of a conventional ELISA using a similar detection process and a GNP-based commercial rapid kit that is widely used for viral detection. The titer-dependent signal produced in our assay was an intense visible signal (**Figure 3f**). In contrast, rapid kits, which are specifically designed to facilitate naked-eye detection, showed much lower sensitivity for optical signals than this assay. For a more accurate comparison, the intensity obtained using ImageJ software was analyzed based on the S/N ratio, and it was confirmed that our assay had a wider detection range than the commercial kit **(Figure S18)**. Additionally, our system showed

Author Manuscript

This article is protected by copyright. All rights reserved

higher sensitivity and a wider analytical range than ELISA **(Figure S19)**. The detection performances of these diagnostic methods were compared, as shown in **Figure 3e and 3g**. The results suggest that our proposed system enables more sensitive detection within 1 h and with a wider dynamic range than ELISA and commercial rapid kits, underscoring its potential as a naked-eye POCT.

2.5. Real Sample Analysis



Recovery ratio (%)				
	Our assay		Commercial kit	
	Saliva	Nasal	Saliva	Nasal
$10^{5.7}$ EID_{50}/mL	117	107	59	75
$10^{3.7}$ EID_{50}/mL	105	94	N/A	N/A

Figure 4. Real sample analysis. The detection performance of this assay was evaluated using various biological samples, including saliva and nasal solutions, and was compared with that of commercial rapid kit. (a) Schematic illustration of workflow for real sample analysis. (b), (c) The detection signals of H1N1 in PBS, saliva, and nasal solutions were shown corresponding to their respective virus titers ($10^{5.7}$ EID_{50}/mL, $10^{3.7}$ EID_{50}/mL, and blank, respectively) and photograph image was analyzed with Image J software. (d), (e) IAV detection using commercial rapid kits for three separate cases, each prepared using a different biological sample. (f) Signal recovery from environmental samples using our assay and a commercial rapid kit was calculated, with normalization based on the signals obtained from PBS. 'N/A' indicates that the calculation is not applicable. Data (c) and (e) represent mean ± standard deviation with n=3.

Author Manuscript

This article is protected by copyright. All rights reserved

A major challenge in the practical application of diagnostic technologies is the presence of many non-target proteins in analytes collected from test subjects, which can interfere with accurate target detection and necessitates additional purification processes.[46] In this regard, we evaluated the detection performance of the assay using realistic test samples to assess its resistance to potential interference from other substances. Because IAVs are mainly transmitted through biofluids in the respiratory tract, we examined its anti-interference ability in saliva and nasal fluid samples. The environmental mock-up samples were prepared by mixing H1N1 virus stock with biofluid and assayed at two virus titers ($10^{5.7}$ and $10^{3.7}$ EID_{50}/mL) and blank (PBS). We compared the detection signals obtained using our assay with that of the commercial rapid kit through analysis by Image J software as illustrated in **Figure 4a.** The detection signals obtained by our assay in the saliva and nasal fluid environments were similar to those obtained in PBS buffer, which contained no external proteins, as shown in **Figure 4b, c and Figure S20**. The assay results were similar in both the PBS and biological samples**.** These results confirm the high anti-interference ability of this assay and suggest its potential for field use. In comparison, the test results of the commercial rapid kit showed a lower intensity in biological samples than in PBS, as presented in **Figure 4d and 4e.** The difference arises from the fact that, while the rapid kit relies solely on a single host-guest interaction, our assay constitutes a system enabling selective signal amplification through both biotin-avidin binding and host-guest interaction. Hence, even in the presence of interference, signal amplification can proceed seamlessly. In the case of the nasal fluid samples from the commercial rapid kit (**Figure 4d**), even the C-line was inconsistent, which was presumed to be due to the viscosity of the fluid affecting the capillary force and preventing smooth lateral flow.[47] As indicated by the recovery ratio in **Figure 4f,** the developed assay demonstrated greater resistance to interference with biological samples than a commercial rapid kit.

Author Manuscript

This article is protected by copyright. All rights reserved

2.6. Application as a Portable BGNP-Based Diagnostic Platform for On-Site Detection



Figure 5. Application as a portable tool for improving the potential of point-of-care testing (POCT). (a) Schematic illustration of the layer-by-layer (LBL) detection process within a tube and an image depicting the optical signal during cycle 2 (b) Optical images of signal detection in the tube during the first and second amplification cycles, as well as the final signal during cycle 2. (c) The detection signal, measured using the smartphone application, was extracted via the CMYK colorimeter in the application, and expressed as the yellow component among the four channels (cyan, magenta, yellow, and black). (d) The detection signal measured using the microplate reader. (e) The detection signal measured using the Image J software. Data (c)-(e) represent mean ± standard deviation with n=3.

One of the most important features of POCT biosensors in resource-constrained settings is their user-friendliness.[48] Considering this perspective, we expected that the use of immunoplate in practical applications could pose a complexity for general users, along with the multiple steps. Therefore, we confirmed that our system has the potential to be used with simpler operating tools and is applicable as a portable system for onsite diagnosis. We used a microtube for IAV detection because it is small and transparent, which makes it easy to use in colorimetric detection. Moreover, it has a solid substrate that can immobilize antibodies and layer BGNPs without concerns regarding capillary force

This article is protected by copyright. All rights reserved

Author Manuscript

loss owing to several washing steps, unlike paper, another useful material.[49] As shown in **Figure 5a**, a series of amplification processes was conducted in the tube in the same manner as in the immunoplate well, and the signal analysis process was further simplified by taking a picture using a smartphone and analyzing it using the RGB Color Detector smartphone application on the App store. The optical signal was analyzed using the Y intensity of the CMYK colorimeter, which has four channels: cyan (C), magenta (M), yellow (Y), and black (K), as supported by the application. For effective antibody immobilization on a solid substrate, we performed (3-aminopropyl)triethoxysilane (APTES) functionalization to improve the orientation of the monoclonal antibody anchored on the tube.[50] When the detection process was performed in the prepared tube, a significant detection signal was obtained due to the accumulation of BGNPs, as observed in the immunoplate **(Figure 5b)**. The test results observed with the naked eye differed slightly between immunowells and tubes, which we attributed to the structural differences between the curved tubes and relatively flat wells. However, in all analyses conducted using a smartphone, microplate reader, and Image J software, we were able to obtain detection signals corresponding to the virus titer **(Figure 5c-e)**. Notably, the LOD of our portable assay, calculated by image extraction using a colorimetric smartphone application, was $10^{1.48}$ EID_{50}/mL, showing a similar performance to that on flat wells and a more sensitive detection than the commercial rapid kit **(Figure S21)**. The results demonstrate that our designed system is applicable as a high sensitivity, user-friendly portable tool that can potentially be used in POCT.

Author Manuscript

This article is protected by copyright. All rights reserved

3. Conclusions

In summary, we developed a highly sensitive colorimetric detection system using a dual-signal amplification strategy that captures the target virus, creates a layered BGNP structure on its surface, and leverages the enzymatic activity of the BGNP complex. We conducted comprehensive engineering by employing the surface properties of GNPs, aiming to maximize their nanozyme effect while ensuring ample interaction with avidin through biotin modification for layering. By enhancing the target detection signal through repeated incubation cycles of the avidin and BGNP pair and achieving secondary signal amplification via the nanozyme effect of the complex, we effectively addressed the inherent limitation of the weak signal intensity observed in conventional GNP-based diagnostics. Our approach demonstrated a high level of sensitivity, with a low LOD of $10^{1.29}$ EID_{50}/mL, making it 2500 times more sensitive than conventional diagnostic systems. Furthermore, because this system targets the viral surface proteins, it enables detection of intact viruses without the need for lysis or pretreatment, making it highly convenient **(Figure S22)**. Additionally, the diagnostic performance was validated in both flat wells and microtubes. This application aimed to enhance user-friendliness by simplifying the multiple steps and improving accessibility, for the general user, to overcome the shortcomings of using immunoplate as a POCT tool. As a result, it demonstrates its potential for adaptation to different hardware setups suitable for field use while retaining high sensitivity. In conclusion, our diagnostic system not only shows high sensitivity and selectivity in practical diagnostic settings, but also has great potential as a POCT that enables on-site diagnosis, as it only requires highly portable hardware and smartphones. Furthermore, its application can be extended in the diagnosis of other infectious disease viruses, and can thus contribute significantly to the effective management of infectious diseases in the field, establishing it as a diagnostic system applicable to future pandemics.

Author Manuscript

This article is protected by copyright. All rights reserved

4. Experimental Section

Materials: Gold (III) chloride trihydrate, sodium citrate tribasic dihydrate, hydroquinone, polyvinylpyrrolidone (PVP), BSA, Tween 20, Fusayama/Meyer artificial saliva, APTES, N-(3-dimethylaminopropyl)-N′ ethylcarbodiimide hydrochloride (EDC), N-hydroxysulfosuccinimide sodium salt (sulfo-NHS) and Ultra-15 Amicon® Ultra-15 Centrifugal Filter were purchased from Sigma-Aldrich (St. Louis, MO, USA). Artificial nasal fluid was purchased from Biochemazone (Leduc, Cananda). SH-PEG and SH-PEG-biotin (0.4–5 kDa) were purchased from Nanocs (New York, NY, USA). Avidin from egg white and TMB were purchased from Thermo Fisher Scientific (Waltham, MA, USA). Dulbecco's phosphate-buffered saline (DPBS) was purchased from Welgene (Gyeongsan, Republic of Korea). Additionally, H_2SO_4 for stop solution and ethyl alcohol were purchased from Duksan (Ansan, Republic of Korea). Recombinant anti-influenza A H1N1 hemagglutinin antibody (ab281949) was purchased from Abcam (Cambridge, U.K.). Influenza A H1N1 (A/California/04/2009) hemagglutinin/HA antibody (Biotin) and rabbit pAb (11055-RP01-B) and Influenza A H1N1 (A/California/04/2009) Hemagglutinin/HA Antibody, Rabbit pAb (11055-RP01) for ELISA were purchased from Sino Biological Inc. (Beijing, China). HRP-conjugated goat anti-rabbit IgG heavy and light chain antibodies (A120-101P) for ELISA were purchased from Bethyl Laboratories, Inc. (Montgomery, TX, USA). Standard™ Q Influenza A/B Test for comparison with the commercial rapid kit was purchased from SD biosensors (Suwon, Republic of Korea). Moreover, 400-mesh copper grids were purchased from Ted Pella, Inc. (Redding, CA, USA). Microscope cover glass was purchased from Marienfeld (Lauda-Königshofen, Germany), immunoplates were purchased from SPL Life Sciences (Pocheon, Republic of Korea), and PCR tubes were purchased from Axygen Biosciences (Union City, CA, USA). All experiments were conducted using Milli-Q water (18.2 MΩ·cm).

Author Manuscript

This article is protected by copyright. All rights reserved

Synthesis of Size-Dependent GNPs: Gold nanoparticle seeds with a diameter of 12 nm were synthesized using the citrate reduction method.[51] In brief, 1 mL of gold (III) chloride solution (100 mM) was added to 100 mL of sodium citrate aqueous solution (5 mM), which was refluxed in an oil bath at 95 °C with vigorous stirring for 20 min. A red color was obtained after refluxing and stabilizing for 80 min. The GNP seed solution was centrifuged three times at 7000 ×g for 10 min and stored at 4 °C after cooling to room temperature (25 °C). Subsequently, GNPs with diameters of 40 and 60 nm were synthesized from 12-nm GNP seed solutions using hydroquinone as a reducing agent.[52] Furthermore, 100 μL of gold (III) chloride solution and GNP seed solution (250 mM) were dispersed in Milli-Q water to obtain a final volume of 10 mL with stirring at 600 rpm. The volume of GNP seed solution was 1.024 and 0.25 mL for 40-nm and 60-nm GNPs, respectively . Subsequently, 22 μL of sodium citrate was immediately injected after adding 100 μL of hydroquinone (30 mM) and incubated at room temperature for 4 h. Each solution was centrifuged three times at 8000 ×g for 10 min with addition of 0.01% (w/v) PVP solution to stabilize the GNPs. The resulting size-dependent GNP solutions were stored in Milli-Q water at 4 °C for further use.

Fabrication and Characterization of BGNPs: GNPs with a diameter of 12 nm were modified using SH-PEG and SH-PEG-biotin via conventional methods. Each polymer was dissolved in Milli-Q water at a mass ratio 1:0.1 with GNPs. An equal volume of PEG solution was added dropwise to the GNP solution, which was stirred at 450 rpm. The mixture was stirred overnight at room temperature with gentle swirling. The thiol groups of each PEG solution were covalently attached to the gold surface and functionalized the GNPs to PGNPs and BGNPs. The unbound PEG solution was removed by several rounds of centrifugation at 7000 ×g for 10 min. The final solutions were dispersed in Milli-Q water and remained stable for several months. The size distribution and zeta potential of the BGNPs were compared with those of bare GNPs via dynamic light scattering and zeta potential analysis (ELSZ-2000ZS; Otsuka Electronics, Osaka, Japan). The UV-visible spectrum and OD indicative of

Author Manuscript

This article is protected by copyright. All rights reserved

successful BGNP synthesis were measured using a Spectra Max® i3x microplate-reader (Molecular Devices, CA, USA). The spherical morphology and monodispersity of the BGNPs were visualized using transmission electron microscopy; the images were obtained using a JEM–F200 transmission electron microscope (JEOL, Tokyo, Japan). The chemical bonding of BGNPs due to PEGylation by SH-PEG-biotin was confirmed using FTIR (PerkinElmer, MA, USA) and NMR spectroscopy (Bruker, Bremen, Germany). Characteristic absorption peaks were observed for each measurement. A thermogravimetric analyzer (SDT Q600; TA Instruments, DE, USA) was used to calculate the grafting density of each BGNPs capped with SH-PEG-biotin of different molecular weights. Weight loss of BGNPs synthesized using 0.4, 1, 3.4, and 5 kDa SH-PEG-biotin was measured via TGA under nitrogen gas with a constant heating rate of 10 ℃/min and temperature range of 50–600 ℃. The grafting density (σ) of PEG chains on GNPs was calculated using the following formula:

$$= \frac{\frac{4}{3}\pi R_{gold}{}^{3} W_{PEG} \rho_{core} N_A}{4\pi R_{gold}{}^{2} W_{gold} MW_{PEG}}$$

where R is average radius, N_A is the Avogadro number, and W is weight fraction.

Layering Test in Avidin Immobilized Plate: To prepare an avidin immobilized well for use in the control and BGNP layering, 100 µL of 10 µg/mL avidin was incubated at 37 °C for 1 h. Subsequently, the well was washed three times using 200 µL 0.01% Tween 20 (w/v). PGNPs and BGNPs were diluted to 0.075 mg/ml and incubated in 100 µL for 5 min for each experimental case. This was followed by the addition of 10 µg/mL avidin solution with the same volume and incubation time. This cycle was repeated seven times, and the washing step was performed in the same manner for all sample additions. For signal measurement, the OD_{524} of each experimental case (the first amplification signal) was measured. Subsequently, 33 µL of TMB and H_2O_2 at optimized concentrations were added to wells containing 33 µL of milli-Q water to induce catalysis, and the OD_{652} was measured to confirm secondary amplification.

This article is protected by copyright. All rights reserved

Author Manuscript

Preparation of Viruses: The IAV H1N1(A/California/04/2009) with its subtypes H3N2 (A/Philippine/2/82) and H9N2, and NDV were propagated in the allantoic cavity of 11 day-old embryonated chicken eggs. Each virus stock (100 μL) was inoculated into the cavities of chicken eggs. After incubation for 72 h at 37 °C, the eggs were chilled overnight at 4 °C. The allantoic fluid containing the propagated viruses was harvested and purified by centrifugation at 4,000 rpm for 20 min. The supernatants were frozen at −80 °C for long-term storage and future use in the assay. Human coronaviruses NL-63 (HCoV-NL63/CN0601/14) and Flu B (Influenza B/Seoul/32/2011[Yamagata lineage]) were propagated in Madin–Darby canine kidney cells. After incubation for 48 h at 37 °C, the cells were frozen and thawed at -80 ℃ once. The supernatant containing the propagated viruses was collected and purified by centrifugation at 4,000 rpm for 20 min, transferred to new test tubes, and frozen at −80 °C for long-term storage. The prepared viral stocks were used directly in the assay.

Virus Detection Analysis: The H1N1 virus was detected by BGNP layering under optimized conditions. To anchor the capture antibody to the immunoplate, 100 μL of 0.1 μg/mL monoclonal antibody was incubated at 37 °C for 1 h and washed three times with 200 μL DPBS. Subsequently, to prevent non-specific adsorption of avidin and BGNPs, 200 μL of 0.3% BSA solution was incubated for 1 h at 37 °C and washed three times in the same manner. For the pre-amplification step, 100 μL of serially diluted H1N1 virus ($10^{5.5}$–$10^{-0.3}$ EID_{50}/mL) was added to the capture antibody immobilized plate. Additionally, 100 μL of 0.02 μg/mL polyclonal antibody was added for detection. The pre-amplification mixture was incubated for 10 min at room temperature and washed three times, as described above. Avidin and BGNPs were prepared and added at a molar ratio of 3:1 on a pre-amplified plate for first amplification. Each treatment was performed for 5 min at room temperature, and cycle 1 was completed by washing three times with 0.01% Tween 20 washing buffer at each step. When proceeding to cycle 2, 100 μL of Milli-Q water was added to the plate and the first amplification

This article is protected by copyright. All rights reserved

Author Manuscript

value was measured at OD_{524}. After the measurement of first amplification, the plate was emptied, and Milli-Q water, H_2O_2, and TMB were added sequentially at 33 μL. After incubation for 15 min, the second amplification value was measured at OD_{652}. Subsequently, 100 μL of 5 M H_2SO_4 was added to the plate as stop solution, and the final signal was confirmed at OD_{450}. The optical density was measured at each step using a microplate reader and photographed using a smartphone. The LOD for each amplification and cycle were evaluated as previously described. This procedure was used for several viruses to evaluate the selectivity of the BGNP-layering detection system.

Detection of H1N1 in Biological Solutions: To confirm the target virus detection and anti-interference ability of the biological solution, saliva and nasal solutions were prepared. The H1N1 virus was diluted in PBS, saliva, and nasal solution stocks to achieve concentrations of $10^{5.5}$ EID_{50}/mL and $10^{3.5}$ EID_{50}/mL. The 100 μL of prepared target virus solution was applied to an immunoplate with an anchored capture antibody. After incubation for 1 h at 37 °C, the immunoplate washed three times with 200 μL DPBS and detected in cycle 2 by the BGNP-layering detection system. For comparison with the commercial rapid kit, the H1N1 virus, diluted in the same biological solution, was mixed with 100 μL of the elution buffer included in the commercial rapid kit. At this time, the virus titer of the resulting solution was $10^{5.5}$ EID_{50}/mL and $10^{3.5}$ EID_{50}/mL, and 150 μL of the mixed solution was applied onto the sample pad. The commercial rapid kit was incubated within 30 min at room temperature (25 °C) for analysis.

Application of the Virus Detection Process to Another Portable Device: To immobilize the capture antibody in the microtube, we used a well-established method for fixing antibodies to multiple substrates, with slight modifications.[53] The tube was first incubated with 100 μL of ethanol for 5 min and washed with Milli-Q water 5 times. Subsequently, 100 μL of KOH 1% (w/v) was added to the tube for 10 min and washed. This tube was treated with O2 plasma and silanized by incubation with

This article is protected by copyright. All rights reserved

Author Manuscript

100 µL APTES 2% (v/v) at 37 °C for 1 h. The antibodies prepared via the EDC-NHS reaction were then effectively immobilized by incubation at 37 °C in the APTES tube for 1 h. The subsequent detection steps followed the optimized conditions and methods described above.

Imaging Analysis: AFM was used to confirm the pre-amplification step and its change in topography. Images were obtained using an NX-10 microscope (Park Systems, Suwon, Republic of Korea). A microscope cover glass was used as bare glass, and the pre-amplification step described above was conducted in the same manner. Similarly, SEM was used to confirm BGNP assembly according to incubation cycle. The imaging was performed using a JSM-7610F-Plus microscope (JEOL, Tokyo, Japan). A silicon wafer was prepared as bare glass and subjected to the pre-amplification and first amplification steps described above. Additionally, The detection signal of each cycle was photographed using a smartphone (Samsung Galaxy S10). The immuoplates and commercial rapid kits used for diagnosis at each stage were all photographed at the same location. In all diagnostic tests, negative cases were measured alongside positive cases to prevent a decrease in the reliability of detection results caused by environmental factors such as ambient light. The intensities were measured using ImageJ software 1.47v (National Institutes of Health, Bethesda, MD, USA) and RGB Color Detector application 3.0v (Android). Images of the immunoplate and microtube, which completed the detection process, were uploaded and analyzed using each software.

Statistical Analysis: Each experiment was performed in triplicate (n=3) and presented as mean ± standard deviation. All analyses were conducted using GraphPad Prism 8.0 (GraphPad, Boston, MA, USA). Logarithmic regression was performed to obtain the LOD using the following formula: LOD = $mean_{blank}$ + 3 (SD_{blank}). Significant differences were determined using unpaired t-tests from GraphPad Prism 8.0 and are indicated by n.s. (not significant) and asterisks (*, **, ***, and ****).

Author Manuscript

This article is protected by copyright. All rights reserved

Supporting Information

Supporting Information is available from the Wiley Online Library or from the author.

Acknowledgements

S. Haam acknowledges support from the National Research Foundation of Korea (NRF) grant funded by the Korea government (MSIT) (No. RS-2023-00236421) and Korea Environment Industry & Technology Institute (KEITI) through the Technology Development Project for Biological Hazards Management in Indoor Air Project funded by Korea Ministry of Environment (MOE)(No. RE202101004). D. Song acknowledges support from the Bio & Medical Technology Development Program of the National Research Foundation (NRF) funded by the Ministry of Science & ICT (No. 2021M3E5E3080556).

Conflict of Interest

The authors declare no conflict of interest.

Author Contributions

E. Jeong and G. Park contributed equally to this work.

Received: will be filled in by the editorial staff.
Revised: will be filled in by the editorial staff.
Published online: will be filled in by the editorial staff.

Author Manuscript

This article is protected by copyright. All rights reserved

References

[1] G. Neumann, T. Noda, Y. Kawaoka, *Nature* **2009**, 459, 931.

[2] O. World Health, World Health Organization, Geneva **2020.**

[3] W. H. Organization, *sustainable development goals* **2017**, 7.

[4] A. A. Adalja, M. Watson, E. S. Toner, A. Cicero, T. V. Inglesby, *Johns Hopkins Center for Health Security: Baltimore, MD, USA* **2018**, 28.

[5] N. D. Grubaugh, J. T. Ladner, P. Lemey, O. G. Pybus, A. Rambaut, E. C. Holmes, K. G. Andersen, *Nat. Microbiol.* **2019**, 4, 10.

[6] J. S. Long, B. Mistry, S. M. Haslam, W. S. Barclay, *Nat. Rev. Microbiol.* **2019**, 17, 67.

[7] a) W. H. Organization, **2018**; b) J. S. Long, B. Mistry, S. M. Haslam, W. S. Barclay, *Nat. Rev. Microbiol.* **2019**, 17, 67.

[8] K. Domańska-Blicharz, E. Świętoń, A. Świątalska, I. Monne, A. Fusaro, K. Tarasiuk, K. Wyrostek, N. Styś-Fijoł, A. Giza, M. Pietruk, *Euro Surveill.* **2023**, 28, 2300366.

[9] E. Kim, E. K. Lim, G. Park, C. Park, J. W. Lim, H. Lee, W. Na, M. Yeom, J. Kim, D. Song, S. Haam, *Adv. Mater.* **2021**, 33, e2005927.

[10] T. M. Oeschger, D. S. McCloskey, R. M. Buchmann, A. M. Choubal, J. M. Boza, S. Mehta, D. Erickson, *Acc. Chem. Res.* **2021**, 54, 3656.

[11] H. Zhu, H. Zhang, S. Ni, M. Korabečná, L. Yobas, P. Neuzil, *TrAC, Trends Anal. Chem.* **2020**, 130, 115984.

[12] S. Kurkela, D. W. Brown, *Medicine* **2009**, 37, 535.

[13] A. Roberts, R. S. Chouhan, D. Shahdeo, N. S. Shrikrishna, V. Kesarwani, M. Horvat, S. Gandhi, *Front. Immunol.* **2021**, 12, 732756.

[14] P. B. Luppa, C. Müller, A. Schlichtiger, H. Schlebusch, TrAC, Trends Anal. Chem. **2011**, 30, 887.

[15] Y. Manmana, T. Kubo, K. Otsuka, TrAC, Trends Anal. Chem. **2021**, 135, 116160.

[16] Z. Xu, Z. Liu, M. Xiao, L. Jiang, C. Yi, Chem. Eng. J. **2020**, 394, 124966.

[17] W. He, M. You, Z. Li, L. Cao, F. Xu, F. Li, A. Li, Sensors and Actuators B: Chemical 2021, 334, 129673.

[18] R. Zeng, M. Qiu, Q. Wan, Z. Huang, X. Liu, D. Tang, D. Knopp, Anal. Chem. **2022**, 94, 15155.

[19] R. Zeng, H. Gong, Y. Li, Y. Li, W. Lin, D. Tang, D. Knopp, Anal. Chem. **2022**, 94, 7442.

[20] X. Huang, Z. P. Aguilar, H. Xu, W. Lai, Y. Xiong, *Biosens Bioelectron* **2016**, 75, 166.

[21] J. Budd, B. S. Miller, N. E. Weckman, D. Cherkaoui, D. Huang, A. T. Decruz, N. Fongwen, G.-R. Han, M. Broto, C. S. Estcourt, J. Gibbs, D. Pillay, P. Sonnenberg, R. Meurant, M. R. Thomas,

This article is protected by copyright. All rights reserved

Author Manuscript

N. Keegan, M. M. Stevens, E. Nastouli, E. J. Topol, A. M. Johnson, M. Shahmanesh, A. Ozcan, J. J. Collins, M. Fernandez Suarez, B. Rodriguez, R. W. Peeling, R. A. McKendry, *Nature Reviews Bioengineering* **2023**, 1, 13.

[22] H. Harpaldas, S. Arumugam, C. C. Rodriguez, B. A. Kumar, V. Shi, S. K. Sia, *Lab Chip.* **2021**, 21, 4517.

[23] X. Huang, Y. Zhou, L. Ding, G. Yu, Y. Leng, W. Lai, Y. Xiong, X. Chen, *Small* **2019**, 15, 1903861.

[24] D. Lin, J. Wu, H. Ju, F. Yan, Biosens Bioelectron **2013**, 45, 195.

[25] Z. Yu, Y. Tang, G. Cai, R. Ren, D. Tang, Anal. Chem. **2018**, 91, 1222.

[26] Z. Yu, H. Gong, M. Li, D. Tang, Biosens Bioelectron **2022**, 218, 114751.

[27] Q. Hu, S. Gan, Y. Bao, Y. Zhang, D. Han, L. Niu, *J. Mater. Chem. B Mater. Biol. Med.* **2020**, 8, 3327.

[28] C. C. Chang, C. P. Chen, T. H. Wu, C. H. Yang, C. W. Lin, C. Y. Chen, *Nanomaterials (Basel)* **2019**, 9.

[29] X.-M. Ma, M. Sun, Y. Lin, Y.-J. Liu, F. Luo, L.-H. Guo, B. Qiu, Z.-Y. Lin, G.-N. Chen, *Chinese Journal of Analytical Chemistry* **2018**, 46, 1.

[30] R. Hu, K. Sou, S. Takeoka, *Sci. Rep.* **2020**, 10, 18086.

[31] Y. W. Chu, B. Y. Wang, H. S. Lin, T. Y. Lin, Y. J. Hung, D. A. Engebretson, W. Lee, J. R. Carey, *Chem. Commun. (Camb.)* **2013**, 49, 2397.

[32] S. Chen, Z. Yu, Y. Wang, J. Tang, Y. Zeng, X. Liu, D. Tang, Anal. Chem. **2023**, 95, 14494.

[33] Y. Zhang, E. Villarreal, G. G. Li, W. Wang, H. Wang, *J. Phys. Chem. Lett.* **2020**, 11, 9321.

[34] C. Park, E. Kim, G. Park, B. C. Kim, S. Vellampatti, J. W. Lim, S. Lee, S. Chung, S. H. Jun, S. Lee, *Adv. Funct. Mater.* **2023**, 2214603.

[35] J. M. Rabanel, P. Hildgen, X. Banquy, *J. Control. Release* **2014**, 185, 71.

[36] V. G. Panferov, N. A. Ivanov, T. Mazzulli, D. Brinc, V. Kulasingam, S. N. Krylov, *Angew. Chem. Int. Ed. Engl.* **2023**, 62, e202215548.

[37] K. Rahme, L. Chen, R. G. Hobbs, M. A. Morris, C. O'Driscoll, J. D. Holmes, *RSC Adv.* **2013**, 3, 6085.

[38] X. Chen, Y. Liang, W. Zhang, Y. Leng, Y. Xiong, *Talanta* **2018**, 186, 29.

[39] M. A. Aly, K. J. Domig, W. Kneifel, E. Reimhult, *Sensors (Basel)* **2018**, 18.

[40] Y. Tang, Y. Chen, Y. Wu, W. Xu, Z. Luo, H.-R. Ye, W. Gu, W. Song, S. Guo, C. Zhu, *Nano Lett.* **2022**, 23, 267.

[41] C. McVey, N. Logan, N. T. K. Thanh, C. Elliott, C. Cao, *Nano Res.* **2018**, 12, 509.

This article is protected by copyright. All rights reserved

Author Manuscript

[42] a) M. Uz, V. Bulmus, S. Alsoy Altinkaya, *Langmuir* **2016**, 32, 5997; b) Y. Li, H. J. Schluesener, S. Xu, *Gold Bull.* **2010**, 43, 29.

[43] S. K. Bajpai, Y. M. Mohan, M. Bajpai, R. Tankhiwale, V. Thomas, *J. Nanosci. Nanotechnol.* **2007**, 7, 2994.

[44] J. Shen, Y. Li, H. Gu, F. Xia, X. Zuo, *Chem. Rev*. **2014**, 114, 7631.

[45] T. S. Le, S. He, M. Takahashi, Y. Enomoto, Y. Matsumura, S. Maenosono, *Langmuir* **2021**, 37, 6566.

[46] V. B. Rajal, B. S. McSwain, D. E. Thompson, C. M. Leutenegger, B. J. Kildare, S. Wuertz, *Water Res.* **2007**, 41, 1411.

[47] D. Quesada-González, A. Merkoçi, *Biosens Bioelectron* **2015**, 73, 47.

[48] C. S. Kosack, A.-L. Page, P. R. Klatser, *Bull. World Health Organ.* **2017**, 95, 639.

[49] J. E. Abud, E. H. Luque, J. G. Ramos, H. A. Rodriguez, *Protein Expr. Purif.* **2017**, 135, 16.

[50] Y. Jung, J. Y. Jeong, B. H. Chung, *Analyst* **2008**, 133, 697.

[51] J. Kim, M. Yeom, T. Lee, H.-O. Kim, W. Na, A. Kang, J.-W. Lim, G. Park, C. Park, D. Song, *J. Nanobiotechnology* **2020**, 18, 1.

[52] S. D. Perrault, W. C. Chan, *J. Am. Chem. Soc.* **2009**, 131, 17042.

[53] C. K. Dixit, S. K. Vashist, B. D. MacCraith, R. O'kennedy, *Nat. Protoc.* **2011**, 6, 439.

Author Manuscript

This article is protected by copyright. All rights reserved

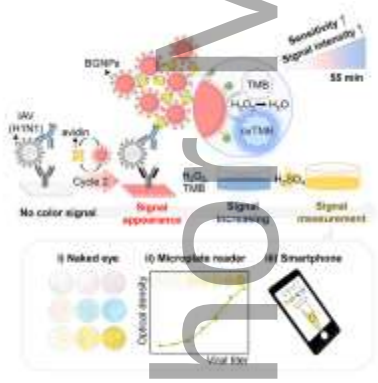
We present an ultrasensitive and visible detection for influenza A virus by leveraging the properties of gold nanoparticles. Dual amplification, achieved through a synthetic nanoprobe utilizing the enzymatic properties of layered gold nanoparticles, exhibits a sensitivity approximately 2,500 times higher than that of conventional immunoassays. This system is demonstrated to be suitable for on-site diagnosis and point-of-care tests within 55 minutes by verifying its diagnostic potential using highly portable devices and smartphones.

Keywords: gold nanoparticle, avidin-biotin binding, nanozyme effect, signal amplification, influenza A virus detection, point-of-care diagnostic

Eunji Jeong, Geunseon Park, Jinyoung Kim, Sojeong Lee, Chaewon Park, Jong-Woo Lim, Minjoo Yeom, Daesub Song,* and Seungjoo Haam*

Ultrasensitive and Visible Detection of Influenza A Virus Based on Enzymatic Properties of Layered Gold Nanoparticles

ToC figure



Author Manuscript

This article is protected by copyright. All rights reserved

Author Manuscript

This article is protected by copyright. All rights reserved